

# Northumbria Research Link

Citation: Mozaffari, Amirpasha, Klotzsche, Anja, Warren, Craig, He, Guowei, Giannopoulos, Antonios, Vereecken, Harry and der Kruk, Jan Van (2020) 2.5D crosshole GPR full-waveform inversion with synthetic and measured data. *Geophysics*. ISSN 0016-8033 (In Press)

Published by: Society of Exploration Geophysicists

URL:

This version was downloaded from Northumbria Research Link:  
<http://nrl.northumbria.ac.uk/id/eprint/43129/>

Northumbria University has developed Northumbria Research Link (NRL) to enable users to access the University's research output. Copyright © and moral rights for items on NRL are retained by the individual author(s) and/or other copyright owners. Single copies of full items can be reproduced, displayed or performed, and given to third parties in any format or medium for personal research or study, educational, or not-for-profit purposes without prior permission or charge, provided the authors, title and full bibliographic details are given, as well as a hyperlink and/or URL to the original metadata page. The content must not be changed in any way. Full items must not be sold commercially in any format or medium without formal permission of the copyright holder. The full policy is available online: <http://nrl.northumbria.ac.uk/policies.html>

This document may differ from the final, published version of the research and has been made available online in accordance with publisher policies. To read and/or cite from the published version of the research, please visit the publisher's website (a subscription may be required.)



UniversityLibrary



**Northumbria**  
**University**  
NEWCASTLE

Confidential manuscript submitted to *Geophysics*  
2.5D crosshole GPR full-waveform inversion

1     **2.5D crosshole GPR full-waveform inversion with synthetic and measured data**

2

3

4     Amirpasha Mozaffari<sup>1,2</sup> (a.mozaffari@fz-juelich.de), Anja Klotzsche<sup>1,2</sup> (a.klotzsche@fz-juelich.de),  
5     Craig Warren<sup>3</sup> (craig.warren@northumbria.ac.uk), Guowei He<sup>1,2</sup> (g.he@fz-juelich.de), Antonios  
6     Giannopoulos<sup>4</sup> (A.Giannopoulos@ed.ac.uk), Harry Vereecken<sup>1,2</sup> (h.vereecken@fz-juelich.de), Jan van  
7     der Kruk<sup>1,2</sup> (j.van.der.kruk@fz-juelich.de)

8

9     <sup>1</sup> Agrosphere (IBG-3), Institute of Bio- and Geosciences, Forschungszentrum Jülich GmbH, Germany

10    <sup>2</sup> Centre for High-Performance Scientific Computing in Terrestrial Systems (TerrSys), Geoverbund  
11    ABC/Jülich, Germany

12    <sup>3</sup> Department of Mechanical and Construction Engineering, Northumbria University, Newcastle upon  
13    Tyne, United Kingdom

14    <sup>4</sup> Institute for Infrastructure and Environment, School of Engineering, The University of Edinburgh,  
15    Edinburgh, United Kingdom

16

17    Running Head: 2.5D GPR full-waveform inversion

18    Corresponding author: Amirpasha Mozaffari

19

Confidential manuscript submitted to *Geophysics*  
2.5D crosshole GPR full-waveform inversion

20

21 **Abstract**

22 Full-waveform inversion (FWI) of cross-borehole Ground Penetrating Radar (GPR)  
23 data is a technique with the potential to investigate the subsurface structures. Typical FWI  
24 applications transform the 3D measurements into a 2D domain via an asymptotic 3D to 2D data  
25 transformation, widely known as a *Bleistein filter*. Despite the broad use of such a  
26 transformation, it requires some assumptions that make it prone to errors. Although the  
27 existence of the errors is known, previous studies have failed to quantify the inaccuracies  
28 introduced on permittivity and electrical conductivity estimation. Based on a comparison of 3D  
29 and 2D modeling, errors could reach up to 30% of the original amplitudes in layered structures  
30 with high contrast zones. These inaccuracies can significantly affect the performance of the  
31 crosshole GPR FWI in estimating permittivity and especially electrical conductivity. We  
32 addressed these potential inaccuracies by introducing a novel 2.5D crosshole GPR FWI that  
33 utilizes a 3D finite-difference time-domain forward solver (*gprMax3D*). This allows us to  
34 model GPR data in 3D, while carrying out FWI in the 2D plane. Synthetic results showed that  
35 2.5D crosshole GPR FWI outperformed the 2D FWI by achieving higher resolution and lower  
36 average errors for permittivity and conductivity models. The average model errors in the whole  
37 domain were reduced by around 2% for both permittivity and conductivity, while zone-specific  
38 errors in high contrast layers were reduced by about 20%. We verified our approach using  
39 crosshole 2.5D FWI measured data, and the results showed good agreement with previous 2D  
40 FWI results and geological studies. Moreover, we analyzed various approaches and found an  
41 adequate trade-off between computational complexity and accuracy of the results, i.e. reducing  
42 the computational effort whilst maintaining the superior performance of our 2.5D FWI scheme.

Confidential manuscript submitted to *Geophysics*  
2.5D crosshole GPR full-waveform inversion

43 **Key words:** *Ground penetrating radar, Waveform inversion, Numerical modelling, Wave*  
44 *propagation*

Confidential manuscript submitted to *Geophysics*  
2.5D crosshole GPR full-waveform inversion

45 **Main Body**

46 INTRODUCTION

47 Crosshole Ground Penetrating Radar (GPR) has gained popularity amongst geophysical  
48 methods for high resolution tomography of the near surface in a wide field of applications in  
49 last three decades (Hubbard et al., 1997; Slater et al., 1997; Tronicke and Holliger, 2004; Looms  
50 et al., 2008; Doetsch et al., 2010; Dorn et al., 2011). Traditionally, travel times from crosshole  
51 GPR data are used to estimate the velocity of the electromagnetic waves between the boreholes,  
52 where the velocity in the medium is inversely proportional to the relative permittivity  $\epsilon_r$  (Annan,  
53 2009). Amplitudes from first arrival picks can be processed to estimate the attenuation of the  
54 electromagnetic waves, where the attenuation is associated with the electrical conductivity  $\sigma$  of  
55 the medium. A standard approach to derive tomographic images of the subsurface is to apply a  
56 ray-based inversion (RBI) that only considers the first arrivals of the waves and corresponding  
57 first cycle amplitudes, which are a relatively small fraction of the information contained in the  
58 recorded traces (Holliger et al., 2001; Holliger and Maurer, 2004). Moreover, the resolution of  
59 the RBI tomogram is scaled by the first Fresnel zone  $\sqrt{\lambda L}$ , where  $\lambda$  is wavelength and  $L$  is the  
60 total path. Therefore, RBI is mostly reliable for models that have a small variation of medium  
61 properties relative to the wavelength, and struggles with presence of high contrast layers  
62 (Stratton, 2015; Williamson, 1991; Rector and Washbourne, 1994; Brenders and Pratt, 2007).

63 Tarantola (1984) was one of the first who introduced the high-fidelity data fitting  
64 technique for seismic data known as full-waveform inversion (FWI). In contrast to RBI, FWI  
65 includes the entire waveform (or at least the first few cycles) of the signal, and its resolution  
66 approaches half of the dominant wavelength or better. As a rule of thumb, by moving from RBI  
67 to FWI, the spatial resolution can improve by up to one order of magnitude for and for borehole  
68 applications, it can reach to one of borehole logging methods (Wu and Toksöz, 1987; Dickens,

Confidential manuscript submitted to *Geophysics*  
2.5D crosshole GPR full-waveform inversion

69 1994; Pratt and Shipp, 1999; Dessa and Pascal, 2003; Belina et al., 2009; Virieux and Operto,  
70 2009; Warner et al., 2013). Since the pioneering work by Tarantola (1984), a large number of  
71 FWI approaches for acoustic and elastic waves have been proposed using time-domain,  
72 frequency-domain, and hybrid methods (Sirgue et al., 2008; Butzer et al., 2013; Lavoué et al.,  
73 2013; Warner et al., 2013; Agudo et al., 2016). Despite the existence of an elastic solution for  
74 crosshole seismic FWI, many applications are still restricted to acoustic-wave solutions due to  
75 the high computational costs of both the forward modeling and inversion (Pratt et al., 1998;  
76 Hollender et al., 1999; Ernst et al., 2007a; Butzer et al., 2013). Within the last decade, FWI was  
77 adapted for electromagnetic wave propagation, especially for crosshole GPR (detailed  
78 overview by Klotzsche et al., 2019). Because finite-difference solutions of Maxwell's equations  
79 are computationally comparable to those of the viscoacoustic-wave equations in seismic, most  
80 of the applications of GPR FWI used a 2D FDTD forward modeling (Ernst et al., 2007a; Meles  
81 et al., 2010). Kuroda et al. (2007) introduced a time-domain 2D FWI to obtain  $\varepsilon_r$  by performing  
82 synthetic studies. Ernst et al. (2007a, 2007b) developed a 2D FWI that utilize a gradient-based  
83 method to obtain high resolution  $\varepsilon_r$  and  $\sigma$  tomograms, and applied it to synthetic and  
84 experimental data. Meles et al. (2010) extended the approach of Ernst et al. (2007a) by  
85 incorporating the vector-based properties of the electromagnetic fields into the FWI, and  
86 simultaneously updating  $\varepsilon_r$  and  $\sigma$ . Next to the time-domain approaches, several frequency-  
87 domain FWI approaches have been developed in the last few years. For example, Lavoué et al.  
88 (2014) proposed a frequency-domain 2D FWI that could reconstruct the  $\varepsilon_r$  and  $\sigma$  of multi-offset  
89 GPR for a synthetic model.

90 The first application of 2D crosshole GPR FWI to experimental data based on Meles et  
91 al. (2010) was performed by Klotzsche et al. (2010). Since this initial application, FWI has been  
92 continuously developed to enhance the application to experimental data and multiple field  
93 applications have been conducted, including the characterization of aquifers (Klotzsche et al.,

Confidential manuscript submitted to *Geophysics*  
2.5D crosshole GPR full-waveform inversion

94 2013; Gueting et al., 2017), karst (Keskinen et al., 2017), and clayey till (Looms et al., 2018).  
95 Studies related to the Widen site (Klotzsche et al., 2013) and the Boise hydrogeophysical test  
96 site (Klotzsche et al., 2014) specifically indicated the potential of FWI to obtain high-resolution  
97 subsurface images including high-contrast layers that were not able to be detected by RBI. Such  
98 layers are important to accurately map and detect, because they can be linked to hydrologically  
99 relevant features such as high porosity zones, preferential flow paths, and impermeable clay  
100 lenses that can significantly effect to flow and transport characteristic of aquifers. High  
101 resolution 2D forward modeling demonstrates that such high contrast layers, related to an  
102 increased  $\epsilon_r$ , can act as low-velocity waveguides causing late arrival high amplitude events in  
103 the data. An overview of the current state-of-the-art of crosshole GPR FWI and its application  
104 to experimental data is provided by Klotzsche et al. (2019).

105 All of the applications of crosshole GPR FWI to experimental data were carried out  
106 with a computationally attractive 2D forward model. FWI using a complete 3D model with  
107 realistic model size requires significantly higher computational resources and large memory  
108 requirements. Wave propagation in 2D and 3D media have differences in its geometrical  
109 spreading, phase, and frequency scaling characteristics. It is necessary to take these differences  
110 into account before using a 2D forward model to invert measured data obtained in a 3D  
111 environment (Ernst et al., 2007a; Brossier et al., 2009; Červený and Pšenčík, 2011; Watson,  
112 2016). The normally applied 2D assumptions are valid as long as there is no out-plane arrival  
113 in the data and in the far-field regime. Any numerical or analytical solution for the 2D wave  
114 equation inherently carries the assumption that any source is a line source, i.e., that it extends  
115 infinitely out-of-plane, causing a cylindrical wave front expanding from the center line. In a 3D  
116 homogenous medium a realistic point source generates a spherical wave front. The difference  
117 in the geometrical spreading of the wave in 2D and 3D media leads to a different amplitude  
118 decay with distance  $r$  and time. In the 3D medium, the energy is spread over the surface of a



Confidential manuscript submitted to *Geophysics*  
2.5D crosshole GPR full-waveform inversion

119 sphere. Hence the amplitude is scaled with  $1/r$ . Whereas in the 2D environment, the energy is  
 120 distributed over the surface of a cylinder, so the amplitude is scaled with  $1/\sqrt{r}$ . Therefore, an  
 121 identical pulse will decay faster in the 3D medium. These differences in geometrical spreading  
 122 also create phase differences between the 2D and 3D Green's functions. In 2D, the Green's  
 123 function is scaled with  $1/\sqrt{\omega}$  compared to 3D, which results in a  $\pi/4$  phase shift between the  
 124 wave solutions for the 3D and 2D environments (Williamson and Pratt, 1995; Červený, 2001;  
 125 Miksat et al., 2008; Červený and Pšenčík, 2011). The differences in geometrical spreading in  
 126 the 2D and 3D environments and the effects on the associated amplitudes and phases should be  
 127 accounted for prior to the inversion. The most common practice to address this issue is to apply  
 128 a 3D to 2D transformation to the field data, referred to as a "geometrical spreading correction"  
 129 (Crase et al., 1990; Červený, 2001; Bleibinhaus et al., 2009; Mulder et al., 2010). The crosshole  
 130 configurations restrict a transmitter and a receiver to a single plane, with the implicit assumption  
 131 that there is negligible variation in the properties of the embedding medium in the direction  
 132 normal to this plane (Song and Williamson, 1995). Bleistein (1986) calculated out-of-plane  
 133 spreading factors using asymptotic theory and approximate asymptotic transformation for  
 134 converting recorded seismic wave fields in a restricted 3D environment to two dimensions.  
 135 Bleistein assumed that acoustic waves propagate in the far-field regime and that the medium  
 136 properties of the host change smoothly. It is formulated in the frequency domain (where  $\omega$  is  
 137 the angular frequency) as:

$$\bar{G}^{2D}(\omega) = \bar{G}^{3D}(\omega) \exp\left[\omega\left(\frac{i\pi}{4}\right)\right] \sqrt{\frac{2\pi L}{|\omega|}}, \quad (1)$$

138 where  $\bar{G}$  is the Green's function of the 2D and 3D media.  $L$  denotes the integral of the velocity  
 139 with respect to the arc-length of the ray trajectory that, in the homogeneous medium, is equal  
 140 to the velocity  $v$  multiplied by the distance  $r$  between the transmitter and receiver  $L = vr$ . This

Confidential manuscript submitted to *Geophysics*  
2.5D crosshole GPR full-waveform inversion

141 asymptotic transformation of restricted 3D to 2D is often termed the “*Bleistein filter*” and is  
142 commonly applied in seismic data processing. Ernst et al. (2007b) adapted this transformation  
143 to electromagnetic wave propagation in the frequency domain as follows:

$$\hat{\mathbf{E}}^{2D}(\mathbf{x}_s, \mathbf{x}_r, \omega) = \hat{\mathbf{E}}^{obs}(\mathbf{x}_s, \mathbf{x}_r, \omega) \sqrt{\frac{2\pi T(\mathbf{x}_s, \mathbf{x}_r)}{-i\omega \varepsilon_r^{mean} \mu_0}}, \quad (2)$$

144 where  $\hat{\mathbf{E}}^{3D}$  are the observed 3D field data and  $\hat{\mathbf{E}}^{2D}$  the transformed 2D data for each transmitter  
145  $\mathbf{x}_s$  and receiver  $\mathbf{x}_r$  location, respectively.  $T$  is the travel time between the transmitter and receiver  
146 positions,  $i^2 = -1$ ,  $\varepsilon_r^{mean}$  is the mean of the relative permittivity of the media, and  $\mu_0$  is the  
147 magnetic permeability of free space. Despite the benefits of the asymptotic 3D to 2D  
148 transformation in avoiding the requirement for computationally intensive 3D modeling, it still  
149 has some shortcomings. The transformation only uses the first-arrival times  $T$  and may perform  
150 poorly for multiple later arrivals. Auer et al. (2013) study the performance of the asymptotic  
151 transformations for seismic crosshole data and show that substantial errors are observed in data  
152 from overlapping arrivals and curved paths. These errors translate into poor model  
153 reconstruction using FWI. Ernst et al. (2007b) claimed a satisfactory performance of the  
154 asymptotic 3D to 2D transformation for experimental data in a far-field regime, but did not  
155 provide a quantitative analysis of the accuracy. Van Vorst et al. (2014) state a good performance  
156 of the asymptotic 3D to 2D transformation for GPR data for travel times, but observed high  
157 inaccuracy in the amplitude transformation that critically influenced the associated  $\sigma$ .  
158 Therefore, more research is required to quantify the effects of the asymptotic 3D to 2D  
159 transformation on 2D GPR FWI, and specifically investigate the electrical conductivity results  
160 in the presences of high contrast zones.

161 In this paper, we first present a numerical modeling study aimed at quantifying the travel  
162 time and amplitude differences between true 2D, and 3D to 2D transformed GPR crosshole

Confidential manuscript submitted to *Geophysics*  
2.5D crosshole GPR full-waveform inversion

163 data. We study the performance of the asymptotic 3D to 2D transformation in complex  
164 structures, and propose using 3D forward modeling to mitigate inaccuracies in the crosshole  
165 FWI to enhance resolution and quantify of the  $\epsilon_r$  and  $\sigma$  results. Therefore, we coupled a 3D  
166 FDTD forward modeling package with our 2D FWI scheme based on Meles et al. (2010)  
167 proposing a 2.5D FWI. The performance of this novel 2.5D FWI is tested and verified using  
168 synthetic and experimental data.

169 EFFECTS OF THE GEOMETRICAL SPREADING CORRECTION

170 To quantify the influence of the asymptotic 3D to 2D transformation on the  
171 experimental data and hence the crosshole GPR FWI results, we first performed a numerical  
172 study to estimate possible errors introduced by this transformation. Previous studies (Auer et  
173 al., 2013; Van Vorst et al., 2014) indicated that the functionality of this transformation is  
174 sensitive to the degree of complexity of subsurface structures. Therefore, we designed a typical  
175 aquifer model including an unsaturated and saturated domain to study the effect of overlapping  
176 arrivals caused by the significant difference in velocity of the electromagnetic waves in  
177 unsaturated and saturated zones. Greenhalgh et al. (2007) showed that the change of acoustic  
178 wave velocity influences the performance of the asymptotic transformation more than the  
179 change in the amplitude through the interface. Because of analogous relations between visco-  
180 acoustic and electromagnetic wave propagation, the translation of this statement for  
181 electromagnetic waves is that the contrast of the  $\epsilon_r$  values before and after the interface is more  
182 important than a change of the  $\sigma$ . Therefore, we limited our studies to models with variations  
183 in the  $\epsilon_r$  and constant  $\sigma$ . We used a 2D FDTD (Meles et al., 2010) and a 3D FDTD (Warren et  
184 al., 2016) algorithm to compute the 2D and 3D data. Both codes use perfect matched layer  
185 (PML) boundaries (Berenger, 1994) to truncate the computational domain, and to simulate the  
186 open boundary nature of the GPR problem. Both algorithms also enforce the CFL stability  
187 condition for FDTD (Hagness and Taflove, 1997). We apply equation 2 to transform the 3D

Confidential manuscript submitted to *Geophysics*  
2.5D crosshole GPR full-waveform inversion

188 data to 2D (which we term ‘*semi-2D*’). The 2D model has the size 11 m x 6 m with boreholes  
 189 5 m apart located at 0.5 m and 5.5 m. The 3D model used the same dimensions as the 2D model  
 190 and was extended by 1.2 m in the transverse direction with the same model parameters as the  
 191 2D plane. The numerical setup contains 11 transmitters and 65 receivers that are placed in the  
 192 two opposite boreholes, from which one specific pair is located in a high contrast zone. Both  
 193 models used a uniform grid with a 3 cm spatial discretization in all dimensions. Figure 1  
 194 highlights a single transmitter (no. 4) and receiver (no. 21) pair (red crosses) in four different  
 195 media configurations. Models (a), (b) and (c) present water saturated scenarios, while model  
 196 (d) illustrates the interaction between the unsaturated and saturated zone. Models (a) and (b)  
 197 are chosen to be homogenous with  $\epsilon_r$  values of 12 and 18, respectively. Model (c) is  
 198 homogenous with a  $\epsilon_r$  of 12 including a lateral structure with a thickness of 1 m and a  $\epsilon_r$  of 18  
 199 located in the middle of the domain. This lateral layer acts as a low velocity waveguide that  
 200 traps the emitted EM wave in this layer and causes multiple late arrival high amplitudes in the  
 201 data (Klotzsche et al., 2014). Model (d) is extended from model (c) considering the unsaturated  
 202 zone with a  $\epsilon_r = 5$ . All four models have a homogenous  $\sigma$  with a constant value of 9.5 mS/m  
 203 ( $\sim 105 \Omega m$ ). As source wavelet we used a predefined wavelet similar to the studies of  
 204 Klotzsche et al. (2012) with a center frequency of 92 MHz for all the models.

205 The left column of Figure 1 shows the simplest possible ray-paths for each model, and  
 206 the corresponding received waveforms are marked with the same number in the center column.  
 207 The shape of the semi-2D waveform is produced by equation 2. To compare the amplitudes of  
 208 the true 2D and the semi-2D waveforms, we scaled the semi-2D waveform to the maximum  
 209 amplitude of 2D  $A_{max}^{2D}$  in the homogeneous cases (a) and (b), and, we use the same scaling factor  
 210 for the models (c) and (d). Note the amplitude of the 3D waveforms have also been scaled for  
 211 visualization purposes. It is clear that there is a good fit between the true 2D and semi-2D  
 212 waveforms for the simple homogenous cases (a) and (b). The ratio of  $A_{max}^{2D} / A_{max}^{semi-2D}$  is almost

Confidential manuscript submitted to *Geophysics*  
2.5D crosshole GPR full-waveform inversion

213 identical for models (a) and (b), despite the fact that there is a 50% difference in  $\epsilon_r$  values of  
214 the two models. This result confirms the previous studies of Ernst et al. (2007b) and Van Vorst  
215 et al. (2014), where they claimed the good performance of the asymptotic 3D to 2D  
216 transformation for simple cases. In contrast, a significant misfit is observed between the 2D and  
217 semi-2D traces for the models (c) and (d) with a higher degree of complexity. In the model (c)  
218 multiple reflections in the waveguide structure cause later arrivals of the waves (6 ns to 12 ns).  
219 The energy distribution is also changed because the first arrival wave has less energy, and the  
220 trapped late arrival waves carry most of the energy. The misfit between the waveforms for 2D  
221 and semi-2D models (c) reaches up to 17% when waves traveling on path 1 and 2 interfere. In  
222 model (d) the misfit rises to 20% of the recorded amplitudes for waves traveling along the  
223 curved ray path (labeled 3 in Figure 1k). The maximum misfit occurs for the waves traveling  
224 along ray path 3 which overlaps with the wave traveling along ray path 2. This results in an  
225 amplitude error of 31%. For both model (c) and model (d), the error increases when the arrival  
226 of the different events overlap. It is important to note that the asymptotic 3D to 2D  
227 transformation does not provide the absolute semi-2D amplitude and therefore requires a  
228 scaling factor for homogeneous media.

229         The misfit in the frequency spectra increases with increasing degree of complexity of  
230 the models. These results confirm the findings of Auer et al. (2013) and Van Vorst et al. (2014),  
231 who outlined that the 3D to 2D transformation performs poorly in complex structures, where  
232 overlapping events occur, and that the transformation has a substantial influence on the  
233 amplitude of the semi-2D waveform. This problem is caused by the nature of the asymptotic  
234 3D to 2D transformation approach that relies on the transformation of the first arrival waves  
235 and the assumption that the highest amplitude of the data is associated with this first arrival  
236 event. Therefore, the performance of the transformation for overlapping or late arrival, high  
237 amplitude events is not reliable (Klotzsche et al., 2010). Moreover, the Bleistein (1986)

Confidential manuscript submitted to *Geophysics*  
2.5D crosshole GPR full-waveform inversion

238 asymptotic transformation is based on the assumption of gradually varying medium properties.  
239 Therefore, sudden changes in medium properties, like the waveguide structure in model (c) and  
240 the transition from unsaturated to saturated zones in model (d), violate this assumption and  
241 consequently the asymptotic 3D to 2D transformation exhibits poor performance in these  
242 scenarios. It is important to point out that the asymptotic 3D to 2D transformation was initially  
243 developed to transform the acoustic waves in seismic analyses where far-field conditions almost  
244 always exist. The far-field assumption is potentially valid for the GPR crosshole setup when  
245 there is sufficient distance between the transmitter and receiver boreholes, but it is not valid for  
246 closely spaced boreholes and on-ground GPR (Streich and van der Kruk, 2007). By comparing  
247 the 2D, semi-2D, and 3D frequency spectra, we observe a small downshift in the center  
248 frequency for the semi-2D and 2D compared to the 3D. Červený and Pšenčík (2011) observed  
249 this phenomenon in seismic data, and they claimed it occurs because of differences between  
250 point and line sources. This shift is an important consideration concerning spatial resolution  
251 since the high-frequency data are necessary for detailed imaging of structures.

252 Summarizing, we observed poor performance of the asymptotic 3D to 2D  
253 transformation in complex structures, with amplitude mismatch errors of more than 30%.  
254 Additionally, applying the asymptotic transformation caused a loss of high-frequency content  
255 in the data, which subsequently affected the resolution of the FWI tomogram. Furthermore,  
256 Watson (2016) stated that even with the geometry of the crosshole setup limiting the transmitter  
257 and receiver to a single plane, the out-of-plane scattering is not zero. Therefore, the 2D  
258 modeling approach may not be able to resolve the data thoroughly and can lead to artifacts in  
259 the reconstruction. These shortcomings of the 3D to 2D transformation make it necessary to  
260 move towards 3D modeling for more accurate FWI. Moreover, 3D modeling makes the detailed  
261 finite-length antenna and borehole modeling possible, which could increase the accuracy of the  
262 FWI for experimental data.

Confidential manuscript submitted to *Geophysics*  
2.5D crosshole GPR full-waveform inversion

## 263 NOVEL 2.5 CROSSHOLE GPR FWI METHODOLOGY

### 264 **3D forward model**

265 To reduce the issues arising from the 3D to 2D transformation, we coupled our existing  
266 2D crosshole GPR FWI with a 3D forward modeling kernel. Therefore, we use gprMax, a well-  
267 developed software for simulating electromagnetic wave propagation based on the 3D FDTD  
268 method (Giannopoulos, 2005; Warren et al., 2016). gprMax uses PML to truncate the  
269 computational domain (Berenger, 1994; Allen Taflove, 1995; Giannopoulos, 2012) and is able  
270 to model rough surfaces and the finite-length GPR antennae (Warren and Giannopoulos, 2011).  
271 The 2D setup is extended to a 3D model, by keeping the medium properties invariant in the  
272 direction perpendicular to the plane containing the boreholes (Song and Williamson, 1995),  
273 which are cylindrical objects, producing a 2.5D model (Tabarovsky and Rabinovich, 1996).

### 274 **Inverse Problem**

275 FWI is an ill-posed problem that can be solved by applying a gradient search method  
276 (Meles et al., 2010). The method requires  $\epsilon_r$  and  $\sigma$  starting models with adequate initial  
277 information. Synthetic data based on these starting models need to yield results that are within  
278 half a wavelength ( $\lambda/2$ ) of the measured data throughout the entire domain. If the synthetic  
279 response has more than half a wavelength misfit from the measured data, the synthetic pulse  
280 could fit an earlier or later measured pulse or even skip the whole pulse. This phenomenon is  
281 called “cycle skipping”, where the inversion is trapped in a local minimum and is not able to  
282 converge to the global minima. Therefore, reasonably accurate starting models are a necessity  
283 for successful inversion (Tarantola, 1986; Chunduru et al., 1997; Virieux and Operto, 2009;  
284 Fichtner, 2011; Klotzsche et al., 2012; Warner et al., 2013). The simultaneous vector-based  
285 gradient search method minimizes the cost function  $C$ , or misfit, between the observed and  
286 modeled data using the FDTD forward model.

Confidential manuscript submitted to *Geophysics*  
2.5D crosshole GPR full-waveform inversion

$$C = 0.5 \times \|E^{syn} - E^{obs}\|^2 \quad (3)$$

287 where  $E^{syn}$  and  $E^{obs}$  are the modeled and observed data for all transmitter/receiver pairs within  
 288 a pre-defined time window. The gradients for the  $\varepsilon_r$  and  $\sigma$  are calculated by a zero-lag cross-  
 289 correlation between the back propagated residual wavefield and the modeled data. These  
 290 gradients define the direction that is expected to minimize the misfit function (see equation 3).  
 291 In the next part, optimal step-lengths for  $\varepsilon_r$  and  $\sigma$  are obtained, which are used together with the  
 292 gradients to simultaneously update the  $\varepsilon_r$  and  $\sigma$  models. Details of the calculation of the misfit  
 293 function, the gradient, and the step-length can be found in Meles et al. (2010). This iterative  
 294 procedure continues until the misfit between the observed and modeled data is reduced below  
 295 a specified value. The method requires knowing the excitation source which is not normally the  
 296 case for experimental data unknown (Pratt, 1999). Therefore, it is necessary to estimate the  
 297 effective source using a deconvolution approach. For more details, see Ernst et al. (2007b) and  
 298 Klotzsche et al. (2010).

## 299 CASE STUDY 1: REALISTIC SYNTHETIC MODEL

### 300 **Model description and generating synthetic data**

301 Our first case study investigates the performance of our new 2.5D FWI approach and  
 302 compare the results with the standard 2D FWI. As realistic input models for the 3D forward  
 303 model, we used the final 2D crosshole GPR FWI results of Klotzsche et al. (2012) that includes  
 304 a high  $\varepsilon_r$  zone between 5 m to 6 m depth acting as a low-velocity waveguide (Figure 2). As  
 305 discussed above, such small-scale zones cause problems in the 3D to 2D transformation by  
 306 introducing possible errors especially in the full-waveform  $\sigma$  results. We used these models in  
 307 the 3D FDTD forward solver with a known effective source wavelet to produce 3D realistic  
 308 synthetic GPR data. For the model dimensions we choose a similar setup as Klotzsche et al.



Confidential manuscript submitted to *Geophysics*  
2.5D crosshole GPR full-waveform inversion

309 (2012) with  $7.62 \text{ m} \times 11.67 \text{ m}$  dimensions using a cell size of 3 cm for the forward modeling  
310 and 9 cm for the inversion. We built the 3D computational grid by extending the transverse  
311 direction to 0.9 m (inversion plane in the center) and truncated the domain with 10 cells of PML  
312 at each boundary. A Hertzian dipole point source was used, and all materials were modeled as  
313 lossy dielectrics, i.e. with no frequency dispersive properties. We transformed these 3D  
314 synthetic GPR data into 2D GPR data using the standard 3D to 2D transformation. The source  
315 wavelet for the 2D FWI is updated using the deconvolution approach as proposed by Klotzsche  
316 et al. (2010). Note that this step is necessary to also account for the different radiation patterns  
317 of the 3D and 2D environment. 2D FWI using the transformed data is prone to exhibit poor  
318 performance in determining  $\varepsilon_r$  and  $\sigma$  with a subsurface model that contains thin layers and high  
319 contrasts in medium properties. Hence, two inversions are performed: (1) 2.5 FWI using the  
320 3D data and the known input source wavelet, and (2) 2D FWI using the asymptotic 3D to 2D  
321 data transformation and an updated source wavelet.

## 322 **Starting models**

323 Ray-based inversion can usually provide sufficient information as starting models, by  
324 using first-arrival times and first-cycle amplitudes of the data (Holliger et al., 2001; Maurer and  
325 Musil, 2004) However, Klotzsche et al. (2012) show that ray-based inversion can fail to identify  
326 the major changes in the  $\varepsilon_r$  close to high contrast regions like the water table or small-scale high  
327 contrast layers. Hence, they propose updating the starting model for the  $\varepsilon_r$  by including a  
328 homogeneous zone near the water table and water table itself. Similar to Klotzsche et al. (2012),  
329 we used the starting models based on the ray-based inversion results with an updated zone  
330 between 5 – 6 m depth. For the  $\sigma$  starting model we used a homogenous model similar to  
331 Klotzsche et al. (2012) that represents the mean of the first cycle amplitude inversion with a  
332 value of  $\sigma = 9.5 \text{ mS/m}$ .

Confidential manuscript submitted to *Geophysics*  
2.5D crosshole GPR full-waveform inversion

333 We observed that the 2.5D FWI did not converge using the same starting models as for the 2D  
334 inversion of the synthetic data, while the 2D FWI could successfully reproduce the synthetic  
335 models. We believe there were simultaneous effects from the 3D to 2D transformation that  
336 caused this issue:

- 337 • The 3D to 2D transformation shifts the data on average by 1.5 ns in time (see Figure 1).  
338 Using the 2D ray-based starting models produced data within half a wavelength for the  
339 2D inversion. However, due to this shift, the 3D measured data are more than a half-  
340 wavelength away from the modeled data and therefore could not converge successfully  
341 due to cycle skipping.
- 342 • Because the center frequency of the transformed data using the 3D to 2D transformation  
343 is slightly lower than the original 3D data. This shift indicates that the high-frequency  
344 content in the transformed data is reduced and the transformed data have a lower spatial  
345 resolution compared to the original data. Therefore, it is easier to fit the modeled data  
346 to the transformed data with lower complexity compared to the original measured data  
347 with higher resolution. Thus, synthetic traces produced by the 2D forward model could  
348 fit the transformed data while synthetic traces from the 3D forward model could not  
349 match the original data due to the additional detail present in the 3D model.

350 Therefore, to guarantee an overlap within half a wavelength of the starting model based  
351 synthetic data and the measured data in the entire domain, we updated the  $\epsilon_r$  starting model  
352 with a single homogenous upper layer with a constant value of  $\epsilon_r = 18$  in the depth range 4 m  
353 to 6 m (before in average  $\epsilon_r = 16$ ). This update guaranteed an overlap of half a wavelength in  
354 the entire domain and allowed successful convergence for both 2D and 2.5D FWI.

355 **Inversion strategies**

Confidential manuscript submitted to *Geophysics*  
2.5D crosshole GPR full-waveform inversion

356           2.5D FWI requires almost 300 times more computational CPU-hours than 2D FWI due  
 357 to the computationally intensive 3D modeling. As we have seen the 2.5D FWI is also more  
 358 sensitive to the  $\varepsilon_r$  starting model. Hence, there is a higher chance of the inversion becoming  
 359 trapped in local minima instead of converging to the global minimum. Therefore, alongside the  
 360 conventional FWI (direct method), we studied possible inversion strategies that could reduce  
 361 the required computational effort and increase the chance of a successful convergence (cascade  
 362 method). These cascade methods require the 2D inversion to be stopped in a particular stage,  
 363 and the output is used as a priori information for a new start of the inversion with more detailed  
 364 starting models. Since we knew the expected output from our synthetic study, we were able to  
 365 compare the performance of the 2D FWI (with asymptotic 3D to 2D transformation applied)  
 366 and 2.5D FWI schemes. We quantified the evaluation by calculating the relative model error  
 367 for the  $\varepsilon_r$  and  $\sigma$  independently as follows:

$$\xi(m_{cal})_{\sigma,\varepsilon} = 100 \times \left( \frac{m_{cal} - m_{true}}{m_{true}} \right)_{\sigma,\varepsilon} \quad (4)$$

368 where  $\xi(m_{cal})_{\sigma,\varepsilon}$  is the relative average error (*AE*) in percentage,  $m_{cal}$  and  $m_{true}$  are the  
 369 modeled and reference values for each element in the domain, respectively. As the performance  
 370 of the 2D FWI is prone to inaccuracy in the layered zone, we calculated lateral average error  
 371 (*LAE*) as a function of the depth alongside the *AE* in the whole domain.

### 372 *Direct 2.5D FWI*

373           The  $\varepsilon_r$  and  $\sigma$  tomograms obtained from 2D and direct 2.5D FWI strategy for identical  
 374 starting model are shown in Figure 3. Comparing the results with the reference models (Figure  
 375 2) shows that both 2D and 2.5D FWI were able to qualitatively resolve the main features of the  
 376  $\varepsilon_r$  and the  $\sigma$  tomograms. For the  $\varepsilon_r$  tomograms, both FWIs reconstructed the three main layers

Confidential manuscript submitted to *Geophysics*  
2.5D crosshole GPR full-waveform inversion

377 successfully, while the results of the 2D FWI appear to be smoother than those from the 2.5D  
378 FWI. The  $\sigma$  tomograms are well-reconstructed for both approaches as both results shows main  
379 features of the synthetic input model. Despite the fact that the tomograms look similar from a  
380 qualitative perspective, a quantitative comparison shows differences in accuracy. The 2D FWI  
381 overestimates  $\varepsilon_r$  between 4.2 m - 5.7 m, where the *LAE* reaches 26%. The obtained  $\varepsilon_r$  for the  
382 2.5D FWI fits better the reference model with a maximum *LAE* of 7% at the interface between  
383 the upper high-velocity zone and the low-velocity waveguide. The *AE* in estimated  $\varepsilon_r$  in the  
384 whole domain is 2.5% for 2D FWI, while this value is 0.18% for 2.5D FWI. The *LAE* for  $\sigma$   
385 reached 32% and then dropped to -21% in the transition from high to low  $\sigma$  layers at depths of  
386 5 m to 6 m. The *LAE* for the 2.5D FWI  $\sigma$  has maximum values of +6.5% and -21%. The *AE* for  
387  $\sigma$  in the whole domain is 2.8% for 2D FWI, while this value is 0.5% for 2.5D FWI.

388 To evaluate the performance of the two FWI approaches with the reference model, we compare  
389 two cross-sections (A-A) and (B-B) in each model (indicated in Figure 3). The  $\varepsilon_r$  values in A-  
390 A show a better fit to the reference values for the 2.5D FWI compared to the 2D FWI (Figure  
391 4). While both 2D and 2.5D FWI underestimate the  $\varepsilon_r$  at depths of 8 m to 10 m. The values of  
392  $\sigma$  in A-A reveal a more accurate 2.5D FWI result. In the B-B cross-section,  $\varepsilon_r$  of the 2D FWI  
393 shows significant error in first 1.5 m depth and slightly misplaces the maximum peak. The  $\varepsilon_r$   
394 values for the 2.5D FWI better fit the reference model all along cross-section B-B. The 2D FWI  
395 overestimates the  $\sigma$  in the upper layer and underestimates it continuously in the middle and  
396 lower areas, whereas the 2.5D FWI result was closer to the reference model. Moreover, the  $\varepsilon_r$   
397 and  $\sigma$  model produced with the 2.5D FWI shows higher resolution in comparison to the results  
398 of the 2D FWI while it revealed smaller spatial variation for both  $\varepsilon_r$  and  $\sigma$ . This observation  
399 agrees with our hypothesis previously mentioned that the 2.5D FWI better reconstructs the 3D  
400 input models especially the electrical conductivity results by eliminating the effect of the  
401 asymptotic 3D to 2D data transformation.

Confidential manuscript submitted to *Geophysics*  
2.5D crosshole GPR full-waveform inversion

402 The normalized root mean square (RMS) error for the 2D FWI is reduced to 22% of the initial  
403 value, while this value is reduced to 12% for 2.5D FWI results. Both 2D and 2.5D FWI had  
404 termination criteria to stop the inversion when the change of the RMS error value in two  
405 consecutive iterations was less than 0.5%. The 2D FWI stopped after 21 iterations, while the  
406 2.5D FWI met this criterion after 23 iterations. Note that also a good data fit and no remaining  
407 gradient was present for all inversion results. Our new 2.5D FWI approach exhibits better  
408 performance over the 2D FWI in reconstructing the  $\varepsilon_r$  and  $\sigma$  models, regarding both correct  
409 positioning and accuracy of the assigned values. Furthermore, the  $\varepsilon_r$  and  $\sigma$  models of the 2.5D  
410 FWI have lower  $AE$  than the 2D FWI, and structures are slightly better resolved in the 2.5D  
411 FWI. Despite this superior performance, it is necessary to consider the higher computational  
412 demands of the 3D modeling used in our 2.5D FWI. Computational times for the simulations  
413 mentioned above are given in Table-1.

414 *Cascade 2.5D FWI*

415 As shown in Mozaffari et al. (2016), the results of the 2D FWI with a limited number of  
416 iterations can be used to improve the starting models for the 2.5D FWI, which allows a faster  
417 convergence and hence reduces the computational effort. Therefore, we applied 2D FWI to  
418 create  $\varepsilon_r$  starting models at iterations 1, 4 and 7, and then we used them for the 2.5D FWI. These  
419  $\varepsilon_r$  models were used as starting models and were inverted with the 2.5D FWI (homogenous  $\sigma$   
420 starting model) until change of the misfit between two subsequent iterations is less than 0.5%  
421 (see Figure 5). All three models successfully show the key features and structures of both  $\varepsilon_r$  and  
422  $\sigma$ . Furthermore, the comparison of the  $\varepsilon_r$  and  $\sigma$  results show that  $AE$  and  $LAE$  are increased by  
423 using the starting models that developed for a more extended time by the 2D FWI (see Table  
424 1), indicating an increase in inaccuracies of the tomograms.

Confidential manuscript submitted to *Geophysics*  
2.5D crosshole GPR full-waveform inversion

425 All these results show that the percentage of the  $AE$  increases proportionally with increasing  
426 number of iterations of the 2D FWI used as starting models. Nevertheless, using this method  
427 could have a significant effect on the required computational effort. The computational time for  
428 the total inversion reduced by 5%, 20%, and 35% for the three models respectively, as shown  
429 in Table 1. All computations were carried out on JURECA cluster (Krause and Thörnig, 2016)  
430 , which is part of the Jülich Supercomputing Centre (JSC). It is equipped with 1872 computing  
431 nodes with two Intel Xeon (E5-2680) with 2x12 cores at 2.5 GHz, simultaneous multithreading,  
432 and DDR4 (2133 MHz) memory with various capacities from 128 to 512 GB.

433 *2.5D FWI with updated  $\varepsilon_r$  starting model*

434 We propose a second strategy, where we combine the methods of Klotzsche et al. (2012)  
435 and Mozaffari et al. (2016). Thereby, we update only the  $\varepsilon_r$  starting model with essential  
436 features revealed in the 2D FWI. Note that we checked for each starting model update if the  
437 half-wavelength criterion is still valid by performing forward modeling using these models and  
438 the 3D forward solver, and compared the input and the modeled data. The most significant  
439 missing attribute in the  $\varepsilon_r$  starting model that we used so far is the high  $\varepsilon_r$  layer at a depth of 5.5  
440 m to 6.0 m. This feature is revealed after a limited number of iterations in both the 2D and 2.5D  
441 FWI, while the  $\sigma$  does not show significant changes. Hence, our new updated  $\varepsilon_r$  starting model  
442 consists of two-horizontal layers, where the lower and upper layer have  $\varepsilon_r$  values of 22 and 18,  
443 respectively (Figure 6a).

444 The 2.5D FWI with the updated  $\varepsilon_r$  starting model produced  $\varepsilon_r$  and  $\sigma$  tomograms with  
445 maximum  $LAE$  of 8% and 9%, respectively. These maximums occurred at the interface of the  
446 high  $\varepsilon_r$  layers. The  $AE$  for  $\varepsilon_r$  and  $\sigma$  errors were 0.16% and 0.45%, respectively, which is slightly  
447 better than the 2.5D FWI using the direct approach (compare Figure 6). Using this updated  $\varepsilon_r$   
448 starting model, the 2.5D FWI required 44% less computational time to converge using the same

Confidential manuscript submitted to *Geophysics*  
2.5D crosshole GPR full-waveform inversion

449 number of CPUs. A summary of the 2D FWI and 2.5D FWI using different strategies with  
450 required computational demand is presented in Table 1. Furthermore, by comparing the  
451 convergence of the inversion and the RMS distributions over number of iterations for the  
452 different strategies (Figure 7), it can be noticed that both strategies for the 2.5D FWI result in  
453 the same final RMS value, while updating the  $\varepsilon_r$  starting model helped to reduce the RMS in  
454 earlier iterations of inversion.

455 In summary, despite the fact of the reduction in computational effort by using the  
456 cascaded 2.5D FWI, the final 2.5D FWI results are significantly affected by the 2D FWI  
457 drawbacks. This is because the *AE* is directly linked to the level of development of the starting  
458 model from the 2D FWI. Hence, choosing an adequate starting model based on the 2D FWI  
459 results is a compromise between the computational effort and accuracy of the results. Therefore,  
460 we do not suggest using early-stage results from the 2D FWI as an input for the 2.5D FWI. In  
461 contrast, the proposed method using a  $\varepsilon_r$  starting model for the 2.5D FWI with updates based  
462 on the results of the 2D FWI can significantly reduce the computational effort, while the  
463 accuracy of the models is not affected. We further apply this approach to invert experimental  
464 GPR data from the Widen test site.

465 CASE STUDY 2: EXPERIMENTAL DATA

466 **Test site description**

467 To validate the findings of the synthetic tests, we applied the 2.5D FWI approach to the  
468 experimental data of the Widen site (Switzerland). Several geophysical and hydrological  
469 studies have been performed at this site characterizing the aquifer in detail (Diem et al., 2010;  
470 Doetsch et al., 2010; Coscia et al., 2011). The aquifer comprises a glaciofluvial deposit that  
471 includes a 3 m alluvial loam (silty sand) at the top, a 7 m thick gravel layer, and a low  
472 permeability clay aquitard below 10 m depths (Cirpka et al., 2007). Multiple monitoring wells  
473 with 11.4 cm diameter are installed near to the river Thur. The GPR data were measured with

Confidential manuscript submitted to *Geophysics*  
2.5D crosshole GPR full-waveform inversion

474 a RAMAC Ground Vision system from Mala Geoscience with 250 MHz antennae. The dataset  
475 was acquired in neighboring boreholes on the south-west plane, where the water table was at  
476 approximately 4.2 m depth (Doetsch et al., 2010). As shown in Klotzsche et al. (2012) a high  
477  $\epsilon_r$  (high porosity) zone that could be linked to zones of preferential flow is located between 5  
478 m - 6 m depth.

#### 479 **FWI results**

480 We applied 2.5D FWI to the same dataset as Klotzsche et al. (2012) and used the same  
481 data pre-processing steps, except that the 3D to 2D conversion is not necessary anymore for the  
482 2.5D FWI. The effective source wavelet was updated using the deconvolution approach for the  
483 3D GPR data and compared to the 2D FWI effective source wavelet (Figure 8). Based on the  
484 finding of the synthetic studies, we chose as a starting model for the  $\epsilon_r$  the updated model based  
485 on the 2D features (Figure 6a). A homogenous  $\sigma$  starting model of 9.5 mS/m is used. The  
486 inversion converged and the 16th iteration was estimated as an optimal solution (Figure 9),  
487 where the change of the RMS error compared to the previous iteration was less than 0.5% and  
488 no remaining gradient was present. Unfortunately, we do not have any logging data from the  
489 same boreholes. Therefore, we tried to validate the experimental based on previous studies. The  
490  $\epsilon_r$  and  $\sigma$  tomograms produced by 2.5D FWI are in a good agreement with the 2D FWI results  
491 from Klotzsche et al. (2012). The slightly upward dipping high  $\epsilon_r$  structure between 5.3 m to  
492 6.1 m was identified as low-velocity. We also observed the same structure using our new 2.5D  
493 FWI approach. The average  $\sigma$  values for 2.5D FWI results are around 1.4% lower than the  
494 average values from the 2D FWI. These differences in  $\sigma$  values are higher in zones with higher  
495  $\epsilon_r$  between 5.2 m – 6 m and 9.2 m – 10 m. The RMS misfit error between the measured and  
496 2.5D modeled data was reduced to 50% from the starting model values. In comparison, the 2D  
497 RMS errors for the same starting model only reduced by 48%. The lower average  $\sigma$  in the entire



Confidential manuscript submitted to *Geophysics*  
2.5D crosshole GPR full-waveform inversion

498 domain for 2.5D FWI is the main reason for the 2% improvement in the RMS misfit compared  
499 to the 2D FWI.

500 The computational requirement of the 2.5D FWI is more than 300 times higher than for  
501 the 2D FWI. The small increase in accuracy of the 2.5D FWI for the experimental data is  
502 perhaps not convincing given the high computational effort. Nevertheless, higher accuracy and  
503 less uncertainty for the  $\sigma$  results are achieved by reducing assumptions that mainly affect the  
504 amplitudes, and hence more quantitative results are obtained. Furthermore, 3D modeling will  
505 enable us to model the borehole, borehole-filling, and realistic finite-length antennas in the  
506 future. We expect to make significant improvements in accuracy by including these features in  
507 our future simulations, which will justify the extra computational effort from using 3D forward  
508 models.

509 CONCLUSION

510 In this paper, we have investigated the performance of the asymptotic 3D to 2D  
511 transformation. Despite the usefulness of the asymptotic data transformation to avoid  
512 computationally expensive 3D modeling, it assumes that the highest wave amplitudes are  
513 associated with the first arrival. We demonstrated that this asymptotic transformation function  
514 only works accurately in such simple subsurface cases, while it fails with complex structures  
515 such as high contrast layers that produce overlapping arrivals from several different features.  
516 Moreover, the amplitudes assigned to waves after the 3D to 2D transformation are only valid  
517 for simple homogenous media and are therefore not suitable for non-uniform media. We also  
518 observed that applying the 3D to 2D transformation to measured data lowers the resolution of  
519 the data by reducing the high-frequency content. Therefore, to overcome the restrictions of the  
520 3D to 2D conversion assumptions and to minimize the associated errors in the crosshole GPR  
521 FWI results, we extended the existing 2D FWI with a 3D forward model. Our new 2.5D FWI

Confidential manuscript submitted to *Geophysics*  
2.5D crosshole GPR full-waveform inversion

522 uses gprMax as a complete 3D FDTD modeling engine which makes the 3D to 2D  
523 transformation unnecessary. We compared the performance of 2D FWI (with 3D to 2D  
524 transformation) and the 2.5D FWI for realistic synthetic data. The results for 2.5D FWI showed  
525 higher accuracy in estimated  $\varepsilon_r$  and  $\sigma$  and provided lower AE in tomograms. Thereby, we  
526 observed that the  $\varepsilon_r$  starting model of the 2.5D FWI needed some modifications in comparison  
527 to the 2D starting model to still fit the requirements to provide modeled data within half of the  
528 wavelength of the measured data. The time shifts caused by the asymptotic 3D to 2D  
529 transformation placed the transformed 2D data less than the half-wavelength distance from  
530 modeled data while the original 3D data were too far from modeled data to converge. Moreover,  
531 a slight decrease in the dominant frequency of the transformed data was observed, which caused  
532 a loss of high-frequency content. Despite the lower *AE* and higher resolution of the 2.5D FWI,  
533 the trade-off is a significant increase in computational resources. Therefore, we examined  
534 multiple strategies to improve the starting model by using results from the less computationally  
535 intensive 2D FWI directly. We have studied the possibility of using the 2D FWI intermediate  
536 results as input for 2.5D FWI to reduce the required computational effort. But we found out that  
537 this method will introduce inaccuracies and we have abandoned this idea. Alternatively, we  
538 found that by updating the starting model based on the main features obtained by 2D FWI, we  
539 can reduce the computational costs by more than 40% while maintaining accuracy and  
540 resolution.

541 Finally, we applied the novel 2.5D FWI to previously studied experimental GPR data  
542 from the Widen test site (Switzerland) to investigate changes achieved in the final tomograms.  
543 The results showed agreement with previous 2D works, and all the expected structures were  
544 identified. As expected, the main improvement was that the  $\sigma$  tomogram shows higher values  
545 in zones of higher  $\varepsilon_r$  and high contrast layers. For both synthetic and experimental data, we  
546 have seen that using the ray-based results as starting models for the 2.5D FWI causes the

Confidential manuscript submitted to *Geophysics*  
2.5D crosshole GPR full-waveform inversion

547 inversion to be trapped in a local minimum and an update of the permittivity model was required  
548 to successfully perform the inversion. Overall, we demonstrated that our new 2.5D FWI with  
549 3D forward modeling is a valuable tool for an improved and more quantitative modeling of the  
550 subsurface. In particular, the use of a 3D forward model allows us to reduce assumptions that  
551 mainly affect the quantitative  $\sigma$  results, and, furthermore allows us to simulate important details  
552 including borehole structure, borehole filling, and finite length antennas.

553 ACKNOWLEDGMENTS

554 The authors gratefully acknowledge the computing time granted by the John von Neumann  
555 Institute for Computing (NIC) and provided on the supercomputer JURECA at Jülich  
556 Supercomputing Centre (JSC). We thank Stewart Greenhalgh for helping us in the early stage  
557 of this study. We thank two anonymous reviewers, associate editor, assistant editor Colin  
558 Farquharson and editor in chief Jeffrey Shragge for suggestions and comments that helped us  
559 to improve the paper greatly.  
560

561

Confidential manuscript submitted to *Geophysics*  
2.5D crosshole GPR full-waveform inversion

562 **References**

- 563 Agudo, O. C., N. Vieira, M. Warner, J. Morgan, and I. C. London, 2016, Acoustic full-  
564 waveform inversion in an elastic world: SEG Technical Program Expanded Abstracts  
565 2016, 1058–1062.
- 566 Allen Taflove, 1995, Computational Electrodynamics: The Finite-Difference Time-Domain  
567 Method: Artech House.
- 568 Annan, A. P., 2009, Chapter 1 - Electromagnetic Principles of Ground Penetrating Radar, *in*  
569 H. M. Jol, ed., Ground Penetrating Radar Theory and Applications, Elsevier, 1–40.
- 570 Auer, L., A. M. Nuber, S. A. Greenhalgh, H. Maurer, and S. Marelli, 2013, A critical  
571 appraisal of asymptotic 3D-to-2D data transformation in full-waveform seismic  
572 crosshole tomography: *Geophysics*, **78**, no. 6, R235–R247.
- 573 Belina, F. A., J. R. Ernst, and K. Holliger, 2009, Inversion of crosshole seismic data in  
574 heterogeneous environments: Comparison of waveform and ray-based approaches:  
575 *Journal of Applied Geophysics*, **68**, 85–94.
- 576 Berenger, J. P., 1994, A perfectly matched layer for the absorption of electromagnetic waves:  
577 *Journal of Computational Physics*, **114**, no. 2, 185–200.
- 578 Bleibinhaus, F., R. W. Lester, and J. A. Hole, 2009, Applying waveform inversion to wide-  
579 angle seismic surveys: *Tectonophysics*, **472**, 238–248.
- 580 Bleistein, N., 1986, Two and half dimension in-plane wave propagation: *Geophysical*  
581 *Prospecting*, **34**, 686–703.
- 582 Brenders, A. J., and R. G. Pratt, 2007, Full waveform tomography for lithospheric imaging:  
583 Results from a blind test in a realistic crustal model: *Geophysical Journal International*,

Confidential manuscript submitted to *Geophysics*  
2.5D crosshole GPR full-waveform inversion

- 584       **168**, no. 1, 133–151.
- 585   Brossier, R., S. Operto, and J. Virieux, 2009, Seismic imaging of complex onshore structures  
586       by 2D elastic frequency-domain full-waveform inversion: *Geophysics*, **74**, no. 6,  
587       WCC105–WCC118.
- 588   Butzer, S., A. Kurzmann, and T. Bohlen, 2013, 3D elastic full-waveform inversion of small-  
589       scale heterogeneities in transmission geometry: *Geophysical Prospecting*, **61**, 1238–  
590       1251.
- 591   Červený V., 2001, *Seismic Ray Theory*: Cambridge University Press, 234-416.
- 592   Červený V., and I. Pšenčík, 2011, *Seismic, Ray Theory*, in H. K. Gupta, ed., *Encyclopedia of*  
593       *Solid Earth Geophysics*, Springer Netherlands, 1244–1258.
- 594   Chunduru, R. K., M. K. Sen, and P. L. Stoffa, 1997, Hybrid optimization methods for  
595       geophysical inversion: *Geophysics*, **62**, no. 4, 1196-1207.
- 596   Cirpka, O. a., M. N. Fienen, M. Hofer, E. Hoehn, A. Tessarini, R. Kipfer, and P. K. Kitanidis,  
597       2007, Analyzing bank filtration by deconvoluting time series of electric conductivity:  
598       *Ground Water*, **45**,no. 3, 318–328.
- 599   Coscia, I., S. A. Greenhalgh, N. Linde, J. Doetsch, L. Marescot, T. Günther, T. Vogt, and A.  
600       G. Green, 2011, 3D crosshole ERT for aquifer characterization and monitoring of  
601       infiltrating river water: *Geophysics*, **76**, no. 2, G49–G59.
- 602   Crase, E., A. Pica, M. Noble, J. McDonald, and A. Tarantola, 1990, Robust elastic nonlinear  
603       waveform inversion: Application to real data: *Geophysics*, **55**, 527–538.
- 604   Dessa, J. X., and G. Pascal, 2003, Combined travelttime and frequency-domain seismic  
605       waveform inversion: A case study on multi-offset ultrasonic data: *Geophysical Journal*

Confidential manuscript submitted to *Geophysics*  
2.5D crosshole GPR full-waveform inversion

- 606 International, **154**, 117–133.
- 607 Dickens, T. A., 1994, Diffraction tomography for crosswell imaging of nearly layered media:  
608 *Geophysics*, **59**, 694–706.
- 609 Diem, S., T. Vogt, and E. Hoehn, 2010, Räumliche Charakterisierung der hydraulischen  
610 Leitfähigkeit in alluvialen Schotter-Grundwasserleitern: Ein Methodenvergleich:  
611 *Grundwasser*, **15**, 241–251.
- 612 Doetsch, J., N. Linde, I. Coscia, S. A. Greenhalgh, and A. G. Green, 2010, Zonation for 3D  
613 aquifer characterization based on joint inversions of multimethod crosshole geophysical  
614 data: *Geophysics*, **75**, 53–64.
- 615 Dorn, C., N. Linde, T. Le Borgne, O. Bour, and L. Baron, 2011, Single-hole GPR reflection  
616 imaging of solute transport in a granitic aquifer: *Geophysical Research Letters*, **38**, 1–5.
- 617 Ernst, J. R., H. Maurer, A. G. Green, and K. Holliger, 2007a, Full-Waveform Inversion of  
618 Crosshole Radar Data Based on 2-D Finite-Difference Time-Domain Solutions of  
619 Maxwell ' s Equations: *IEEE Transactions on Geoscience and Remote Sensing*, **45**, no.  
620 9, 2807–2828.
- 621 Ernst, J. R., A. G. Green, H. Maurer, and K. Holliger, 2007b, Application of a new 2D time-  
622 domain full-waveform inversion scheme to crosshole radar data: *Geophysics*, **72**, no 5,  
623 J53.
- 624 Fichtner, A., 2011, Full Seismic Waveform Modelling and Inversion: *Advances in*  
625 *Geophysical and Environmental Mechanics and Mathematics*, 83–88.
- 626 Giannopoulos, A., 2005, Modelling ground penetrating radar by GprMax: *Construction and*  
627 *Building Materials*, **19**, 755–762.

Confidential manuscript submitted to *Geophysics*  
2.5D crosshole GPR full-waveform inversion

- 628 Giannopoulos, A., 2012, Unsplit implementation of higher order PMLs: IEEE Transactions  
629 on Antennas and Propagation, **60**, 1479–1485.
- 630 Greenhalgh, S. A., B. Zhou, D. R. Pant, and A. Green, 2007, Numerical study of seismic  
631 scattering and waveguide excitation in faulted coal seams: Geophysical Prospecting, **55**,  
632 185–198.
- 633 Gueting, N., T. Vienken, A. Klotzsche, J. van der Kruk, J. Vanderborght, J. Caers, H.  
634 Vereecken, and A. Englert, 2017, High resolution aquifer characterization using  
635 crosshole GPR full-waveform tomography: Comparison with direct-push and tracer test  
636 data: Water Resources Research, **53**, 49–72.
- 637 Hagness, S., and A. Taflove, 1997, Finite-Difference Time-Domain (FDTD) Computational  
638 Electrodynamics Simulations of Microlaser Cavities in One and Two Spatial  
639 Dimensions, *in* T. G. Campbell, R. A. Nicolaides, and M. D. Salas, eds., Computational  
640 Electromagnetics and Its Applications, Springer Netherlands, 229–251.
- 641 Hollender, F., S. Tillard, and L. Corin, 1999, Multifold borehole radar acquisition and  
642 processing: Geophysical Prospecting, **47**, 1077–1090.
- 643 Holliger, K., and H. R. Maurer, 2004, Effects of stochastic heterogeneity on ray-based  
644 tomographic inversion of crosshole georadar amplitude data: Journal of Applied  
645 Geophysics, **56**, no. 3, 177–193.
- 646 Holliger, K., M. Musil, and H. R. Maurer, 2001, Ray-based amplitude tomography for  
647 crosshole georadar data: A numerical assessment: Journal of Applied Geophysics, **47**,  
648 285–298.
- 649 Hubbard, S. S., J. E. Peterson, E. L. Majer, P. T. Zawislanski, K. H. Williams, J. Roberts, and  
650 F. Wobber, 1997, Estimation of permeable pathways and water content using

Confidential manuscript submitted to *Geophysics*  
2.5D crosshole GPR full-waveform inversion

- 651 tomographic radar data: *The Leading Edge*, **16**, 1623–1630.
- 652 Keskinen, J., A. Klotzsche, M. C. Looms, J. Moreau, J. van der Kruk, K. Holliger, L.  
653 Stemmerik, and L. Nielsen, 2017, Full-waveform inversion of Crosshole GPR data:  
654 Implications for porosity estimation in chalk: *Journal of Applied Geophysics*, **140**, 102–  
655 116.
- 656 Klotzsche, A., H. Vereecken, and J. van der Kruk, 2019, Review of Crosshole GPR Full-  
657 waveform Inversion of Experimental Data: Recent Developments, Challenges and  
658 Pitfalls: *Geophysics*, **84**, no. 6, H13-H28.
- 659 Klotzsche, A., J. van der Kruk, J. Bradford, and H. Vereecken, 2014, Detection of spatially  
660 limited high-porosity layers using crosshole GPR signal analysis and full-waveform  
661 inversion: *Water Resources Research*, **50**, 6966–6985.
- 662 Klotzsche, A., J. van der Kruk, G. Meles, and H. Vereecken, 2012, Crosshole GPR full-  
663 waveform inversion of waveguides acting as preferential flow paths within aquifer  
664 systems: *Geophysics*, **77**, no. 4, H57.
- 665 Klotzsche, A., J. Jan van der, Kruk, L. Niklas, J. Doetsch, and H. Vereecken, 2013, 3-D  
666 characterization of high-permeability zones in a gravel aquifer using 2-D crosshole GPR  
667 full-waveform inversion and waveguide detection: *Geophysical Journal International*,  
668 **195**, 932–944.
- 669 Klotzsche, A., J. van der Kruk, G. A. Meles, J. Doetsch, H. Maurer, and N. Linde, 2010, Full-  
670 waveform inversion of cross-hole ground-penetrating radar data to characterize a gravel  
671 aquifer close to the Thur River, Switzerland: *Near Surface Geophysics*, **8**, 635–649.
- 672 Krause, D., and P. Thörnig, 2016, JURECA: General-purpose supercomputer at Jülich  
673 Supercomputing Centre: *Journal of Large-Scale Research Facilities JLSRF*, **2**, A62.



Confidential manuscript submitted to *Geophysics*  
2.5D crosshole GPR full-waveform inversion

- 674 Kuroda, S., M. Takeuchi, and H. J. Kim, 2007, Full-waveform inversion algorithm for  
675 interpreting crosshole radar data: A theoretical approach: *Geosciences Journal*, **11**, 211–  
676 217.
- 677 Lavoué, F., R. Brossier, S. Garambois, J. Virieux, and L. Metivier, 2013, 2D full waveform  
678 inversion of GPR surface data: Permittivity and conductivity imaging: IWAGPR 2013 -  
679 Proceedings of the 2013 7th International Workshop on Advanced Ground Penetrating  
680 Radar, **1**.
- 681 Lavoué, F., R. Brossier, L. Métivier, S. Garambois, and J. Virieux, 2014, Two-dimensional  
682 permittivity and conductivity imaging by full waveform inversion of multioffset GPR  
683 data: A frequency-domain quasi-Newton approach: *Geophysical Journal International*,  
684 **197**, no. 1, 248–268.
- 685 Looms, M. C., K. H. Jensen, A. Binley, and L. Nielsen, 2008, Monitoring Unsaturated Flow  
686 and Transport Using Cross-Borehole Geophysical Methods: *Vadose Zone Journal*, **7**,  
687 227.
- 688 Looms, M. C., A. Klotzsche, J. van der Kruk, T. H. Larsen, A. Edsen, N. Tuxen, N.  
689 Hamburger, J. Keskinen, and L. Nielsen, 2018, Mapping sand layers in clayey till using  
690 crosshole ground-penetrating radar: *Geophysics*, **83**,no. 1, A21–A26.
- 691 Maurer, H., and M. Musil, 2004, Effects and removal of systematic errors in crosshole  
692 georadar attenuation tomography: *Journal of Applied Geophysics*, **55**, no. 3-4, 261–270.
- 693 Meles, G. A., J. van der Kruk, S. A. Greenhalgh, J. R. Ernst, H. Maurer, and A. G. Green,  
694 2010, A new vector waveform inversion algorithm for simultaneous updating of  
695 conductivity and permittivity parameters from combination crosshole/borehole-to-  
696 surface GPR data: *IEEE Transactions on Geoscience and Remote Sensing*, **48**, no. 9,

Confidential manuscript submitted to *Geophysics*  
2.5D crosshole GPR full-waveform inversion

697 3391–3407.

698 Miksat, J., T. M. Müller, and F. Wenzel, 2008, Simulating three-dimensional seismograms in  
699 2.5-dimensional structures by combining two-dimensional finite difference modelling  
700 and ray tracing: *Geophysical Journal International*, **174**, no. 1, 309–315.

701 Mozaffari, A., A. Klotzsche, G. He, C. Warren, A. Giannopoulos, H. Vereecken, and J. Van  
702 Der Kruk, 2016, Towards 3D full-waveform inversion of crosshole GPR data: 2016  
703 16th International Conference on Ground Penetrating Radar (GPR), 1-4.

704 Mulder, W. A., C. Perkins, and M. J. Van De Rijzen, 2010, 2D Acoustic Full Waveform  
705 Inversion of a Land Seismic Line: *Eage*, 14–17.

706 Pratt, R. G., 1999, Seismic waveform inversion in the frequency domain, Part 1: Theory and  
707 verification in a physical scale model: *Geophysics*, **64**, no. 2, 888-901.

708 Pratt, R. G., and R. M. Shipp, 1999, Seismic waveform inversion in the frequency domain;  
709 Part 2; Fault delineation in sediments using crosshole data: *Geophysics*, **64**, no. 3, 902–  
710 914.

711 Pratt, R. G., C. Shin, and G. J. Hicks, 1998, Gauss-Newton and full Newton methods in  
712 frequency-space seismic waveform inversion: *Geophysical Journal International*, **133**,  
713 no. 2, 341–362.

714 Rector, J. W., and J. K. Washbourne, 1994, Characterization of resolution and uniqueness in  
715 crosswell direct-arrival travelttime tomography using the Fourier projection slice  
716 theorem: *Geophysics*, **59**, no. 11, 1642–1649.

717 Sirgue, L., J. Etgen, and U. Albertin, 2008, 3D frequency domain waveform inversion using  
718 time domain finite difference methods: 70th EAGE Conference & Exhibition, 9–12.

Confidential manuscript submitted to *Geophysics*  
2.5D crosshole GPR full-waveform inversion

- 719 Slater, L., M. D. Zaidman, M. D. Binley, and L. J. West, 1997, Electrical imaging of saline  
720 tracer migration for the investigation of unsaturated zone transport mechanisms:  
721 *Hydrology and Earth System Sciences*, **1**, no. 2, 291-302.
- 722 Song, Z., and P. R. Williamson, 1995, Frequency-domain acoustic-wave modeling and  
723 inversion of crosshole data: Part I—2.5-D modeling method: , *Geophysics*, **60**, no. 3,  
724 784–795.
- 725 Stratton, J. A., 2015, The Magnetostatic Field: In *Electromagnetic Theory*, 225-267.
- 726 Streich, R., and J. van der Kruk, 2007, Characterizing a GPR antenna system by near-field  
727 electric field measurements: *Geophysics*, **72**, no. 5, A51-A55.
- 728 Tabarovsky, L. A., and M. B. Rabinovich, 1996, 2 . 5-D Modeling in electromagnetic:  
729 *Applied Geophysics*, **35**, no. 4, 261–284.
- 730 Tarantola, A., 1984, Inversion of seismic reflection data in the Acoustic Approximation:  
731 *Geophysics*, **49**, no. 8, 1259–1266.
- 732 Tarantola, A., 1986, A strategy for nonlinear elastic inversion of seismic reflection data:  
733 *Geophysics*, **51**, no. 10, 1893.
- 734 Tronicke, J., and K. Holliger, 2004, Short Note Effects of gas- and water-filled boreholes on  
735 the amplitudes of crosshole georadar data as inferred from experimental evidence:  
736 *Geophysics*, **69**, no. 5, 1255–1260.
- 737 Virieux, J., and S. Operto, 2009, An overview of full-waveform inversion in exploration  
738 geophysics: *Geophysics* , **74**, no. 6, WCC1–WCC26.
- 739 Van Vorst, D. G., M. J. Yedlin, J. Virieux, and E. S. Krebs, 2014, Three-dimensional to two-  
740 dimensional data conversion for electromagnetic wave propagation using an acoustic

Confidential manuscript submitted to *Geophysics*  
2.5D crosshole GPR full-waveform inversion

- 741 transfer function: application to cross-hole GPR data: *Geophysical Journal International*,  
742 **198**, no. 1, 474–483.
- 743 Warner, M., A. Ratcliffe, T. Nangoo, J. Morgan, A. Umpleby, N. Shah, V. Vinje, I. Štekl, L.  
744 Guasch, C. Win, G. Conroy, and A. Bertrand, 2013, Anisotropic 3D full-waveform  
745 inversion: *Geophysics*, **78**, no. 2, R59–R80.
- 746 Warren, C., and A. Giannopoulos, 2011, Creating finite-difference time-domain models of  
747 commercial ground-penetrating radar antennas using Taguchi's optimization method:  
748 *Geophysics*, **76**, no. 2, G37–G47.
- 749 Warren, C., A. Giannopoulos, and I. Giannakis, 2016, gprMax: Open source software to  
750 simulate electromagnetic wave propagation for Ground Penetrating Radar: *Computer*  
751 *Physics Communications*, **209**, 163–170.
- 752 Watson, F., 2016, Towards 3D full-wave inversion for GPR: 2016 IEEE Radar Conference,  
753 RadarConf 2016.
- 754 Williamson, P. R., 1991, A guide to the limits of resolution imposed by scattering in ray  
755 tomography: *Geophysics*, **56**, no. 2, 202-207.
- 756 Williamson, P. R., and R. G. Pratt, 1995, A critical review of acoustic wave modeling  
757 procedures in 2.5 dimensions: *Geophysics*, **60**, no. 2, 591-595.
- 758 Wu, R., and M. N. Toksöz, 1987, Diffraction tomography and multisource holography  
759 applied to seismic imaging: *Geophysics*, **52**, no. 1, 11–25.
- 760
- 761

Confidential manuscript submitted to *Geophysics*  
2.5D crosshole GPR full-waveform inversion

762 **Table Caption:**

763 Table 1. Results of the synthetic study using different inversion strategies and different starting  
764 models *SM*. Maximum lateral average error *LAE* and average error *AE* for the entire domain  
765 between the boreholes for  $\epsilon_r$  and  $\sigma$ . Computation time *CT*, reduction of the computational time,  
766 and RMS reduction normalized to the starting models (SM represented by 100%) for 2D and  
767 2.5D FWI. The bold values indicate the best results.

768

Confidential manuscript submitted to *Geophysics*  
2.5D crosshole GPR full-waveform inversion

769 **Figures Captions:**

770 Figure 1. Synthetic subsurface crosshole GPR setup with: model a) homogenous medium ( $\epsilon_r =$   
771  $12$ ) (1a); model b) homogenous medium ( $\epsilon_r = 18$ ) (1d); model c) homogenous medium ( $\epsilon_r =$   
772  $12$ ) with a waveguide structure ( $\epsilon_r = 18$ ) in the center (1g); and model d) homogenous medium  
773 ( $\epsilon_r = 12$ ) with a waveguide structure ( $\epsilon_r = 18$ ) in the center with an unsaturated zone ( $\epsilon_r = 5$ ) on  
774 top (1j). The transmitter-receiver pairs are marked by red crosses. The corresponding simulated  
775 2D, calculated semi-2D, and 3D traces are in the center column, where the major events are  
776 assigned to possible ray paths by number and dashed purple circles. The frequency spectra are  
777 presented in the right column. Note that the amplitude of the semi-2D and 3D traces are scaled  
778 by the ratio of  $A_{max}^{2D} / A_{max}^{semi-2D}$ .

779 Figure 2. Relative dielectric permittivity (a) and electrical conductivity (b) models based on  
780 Klotzsche et al. (2012) as the simulated reality for synthetic analysis. Note the logarithmic scale  
781 for the  $\sigma$  tomogram. Transmitter and receiver positions are indicated by circle and crosses,  
782 respectively.

783 Figure 3.  $\epsilon_r$  and  $\sigma$  models for 2D (a and b) and 2.5D FWI (c and d), and corresponding lateral  
784 average errors plotted on the left side of the tomograms. A-A and B-B show the positions of  
785 the cross-sections presented in Figure 4. Note the logarithmic scale for  $\sigma$  tomograms.  
786 Transmitter and receiver positions are indicated by circle and crosses, respectively.

787 Figure 4.  $\epsilon_r$  and  $\sigma$  values of the cross-sections A-A (a and b) and B-B (c and d) (position shown  
788 by dotted line in Figure 3) for the reference values (blue), and models produced with 2D (red)  
789 and 2.5D FWI (black).

790 Figure 5.  $\epsilon_r$  and  $\sigma$  and tomograms produced by 2.5D FWI for different starting models created  
791 from the 1<sup>st</sup> (a and b), 4<sup>th</sup> (c and d) and 7<sup>th</sup> (e and f) iteration of 2D FWI. Corresponding lateral

Confidential manuscript submitted to *Geophysics*  
2.5D crosshole GPR full-waveform inversion

792 average errors are plotted on the right side of each tomogram. Note the logarithmic scale for  $\sigma$   
793 tomograms. Transmitter and receiver positions are indicated by circle and crosses, respectively.

794 Figure 6. Updated  $\varepsilon_r$  starting model (a),  $\varepsilon_r$ , (b) and  $\sigma$  (c) resulting tomograms of the 2.5D FWI  
795 and the corresponding lateral average model errors on the left side. Note the logarithmic scale  
796 for  $\sigma$  tomogram. Transmitter and receiver positions are indicated by circle and crosses,  
797 respectively.

798 Figure 7. RMS misfit curves for 2D FWI (blue) and 2.5D FWI (red) using the same starting  
799 models, and, the 2.5D FWI using the updated  $\varepsilon_r$  starting model. RMS curves are normalized to  
800 the starting model value (0 iteration) used for the 2D and 2.5D FWI.

801 Figure 8. Comparison of the 2D effective source wavelet based on Klotzsche et al. (2012) in  
802 red and the 2.5D effective source wavelet in blue using the deconvolution approach. Note both  
803 wavelets are normalized to their maximum amplitude.

804 Figure 9. 2.5D FWI tomograms for  $\varepsilon_r$  (a) and  $\sigma$  (b) for the experimental data of the Widen test  
805 site using the updated starting model (see Figure 6a) and effective source wavelet (see Figure  
806 8, blue). Note the logarithmic scale for  $\sigma$  tomogram. Transmitter and receiver locations are  
807 indicated by circles and crosses, respectively.

808

Table 1. Results of the synthetic study using different inversion strategies and different starting models *SM*. Maximum lateral average error *LAE* and average error *AE* for the entire domain between the boreholes for  $\varepsilon_r$  and  $\sigma$ . Computation time *CT*, reduction of the computational time, and RMS reduction normalized to the starting models (SM represented by 100%) for 2D and 2.5D FWI. The bold values indicate the best results.

FWI strategy	Max. <i>LAE</i> (%) for $\varepsilon_r$	<i>AE</i> (%) of $\varepsilon_r$	Max. <i>LAE</i> (%) for $\sigma$	<i>AE</i> (%) for $\sigma$	CT for 20 iteration (min)	CT reduction compare to 2.5D FWI (%)	RMS reduction normalized to SM (%)
2D	25	2.5	35	2.8	4,5	-	78
2.5D	6	0.18	19	0.5	1196.7	-	88
2.5D – with 1st iteration of the 2D FWI as SM	8	0.21	19	1.0	1136.4	5	84
2.5D – with 4th iteration of the 2D FWI as SM	19	1.55	28	1.6	957.7	20	82
2.5D – with 7th iteration of	23	1.9	33	2.2	778.9	35	81



the 2D FWI as SM							
2.5D with updated SM	<b>8</b>	<b>0.16</b>	<b>11</b>	<b>0.45</b>	<b>664.8</b>	<b>44</b>	<b>88</b>



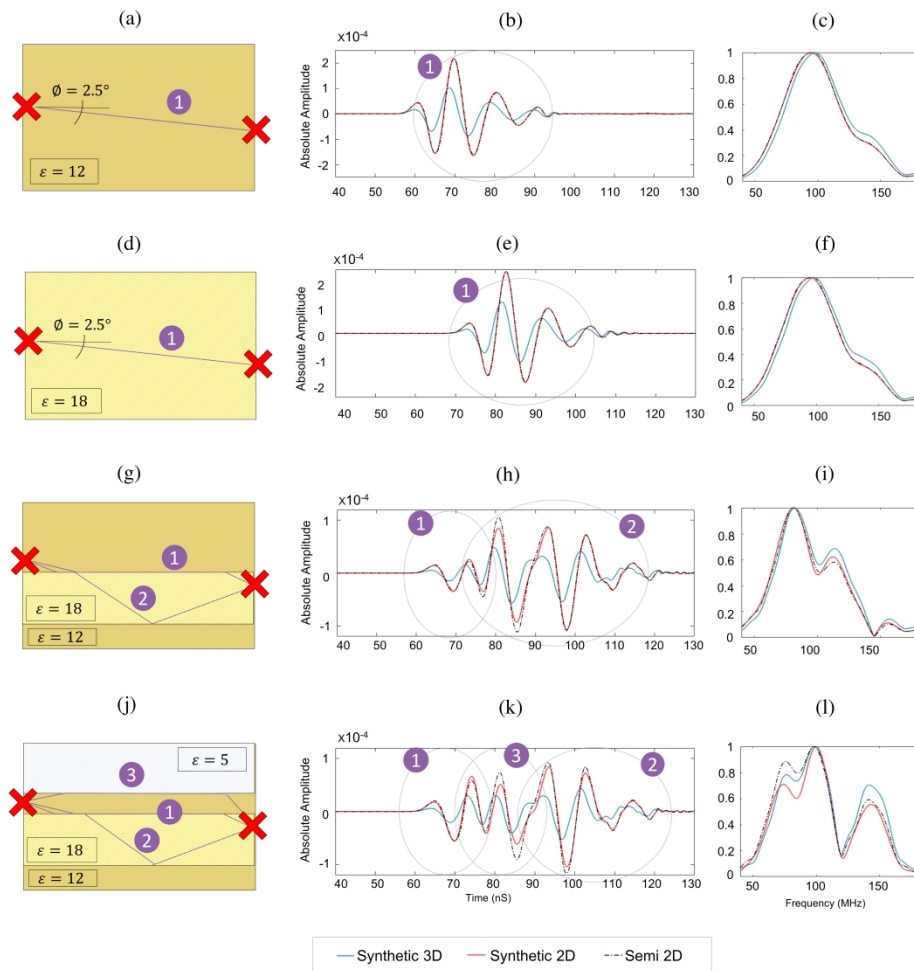


Figure 1 / Synthetic subsurface crosshole GPR setup with: model a) homogenous medium ( $\epsilon_r = 12$ ) (1a); model b) homogenous medium ( $\epsilon_r = 18$ ) (1d); model c) homogenous medium ( $\epsilon_r = 12$ ) with a waveguide structure ( $\epsilon_r = 18$ ) in the center (1g); and model d) homogenous medium ( $\epsilon_r = 12$ ) with a waveguide structure ( $\epsilon_r = 18$ ) in the center with an unsaturated zone ( $\epsilon_r = 5$ ) on top (1j). The transmitter-receiver pairs are marked by red crosses. The corresponding simulated 2D, calculated semi-2D, and 3D traces are in the center column, where the major events are assigned to possible ray paths by number and dashed purple circles. The frequency spectra are presented in the right column. Note that the amplitude of the semi-2D and 3D traces are scaled by the ratio of  $A_{\max}^{2D} / A_{\max}^{\text{semi-2D}}$ .

467x481mm (300 x 300 DPI)

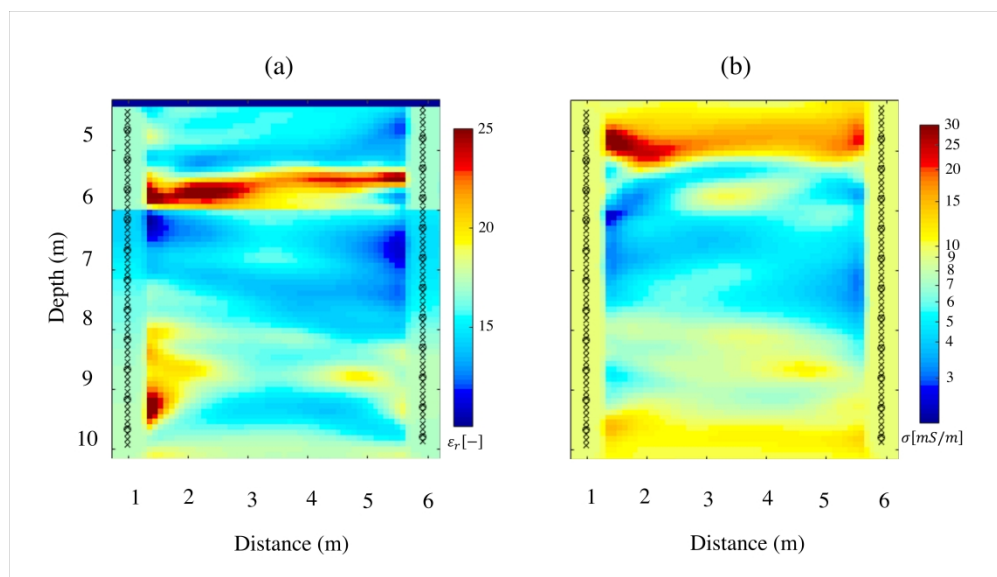
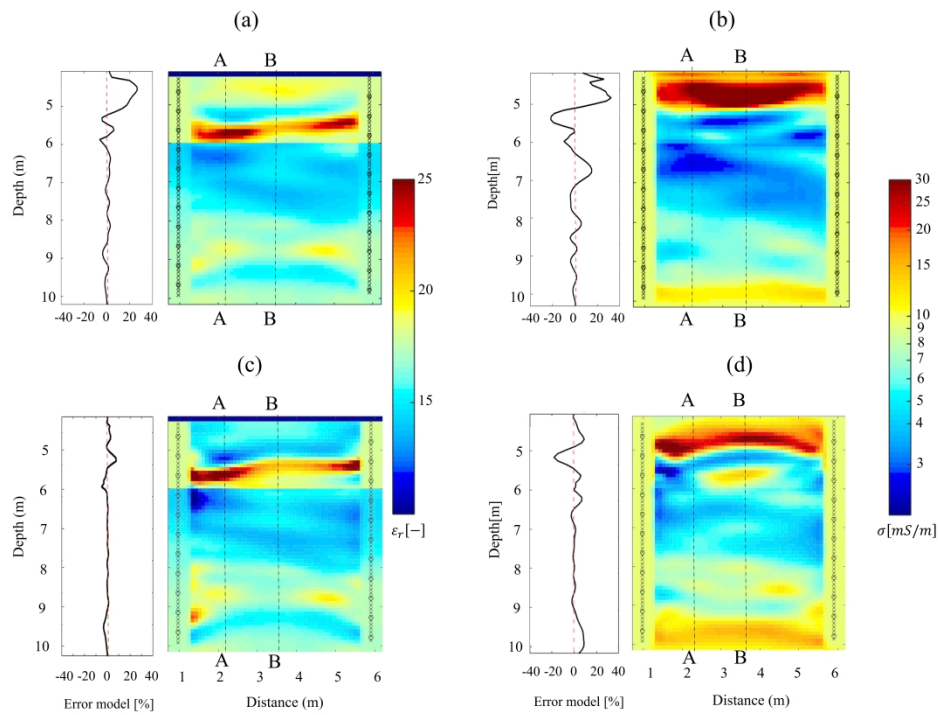


Figure 2 / Relative dielectric permittivity (a) and electrical conductivity (b) models based on Klotzsche et al. (2012) as the simulated reality for synthetic analysis. Note the logarithmic scale for the  $\sigma$  tomogram. Transmitter and receiver positions are indicated by circle and crosses, respectively.

628x361mm (300 x 300 DPI)



Caption : Figure 3 /  $\epsilon_r$  and  $\sigma$  models for 2D (a and b) and 2.5D FWI (c and d), and corresponding lateral average errors plotted on the left side of the tomograms. A-A and B-B show the positions of the cross-sections presented in Figure 4. Note the logarithmic scale for  $\sigma$  tomograms. Transmitter and receiver positions are indicated by circle and crosses, respectively.

558x448mm (300 x 300 DPI)

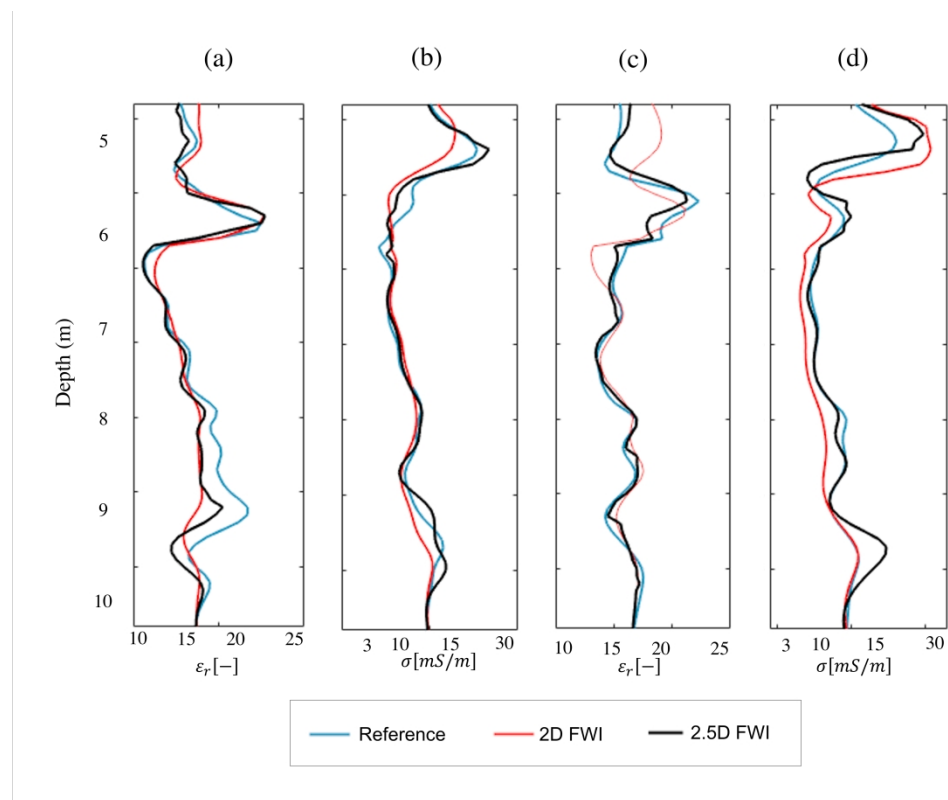


Figure 4 /  $\epsilon_r$  and  $\sigma$  values of the cross-sections A-A (a and b) and B-B (c and d) (position shown by dotted line in Figure 3) for the reference values (blue), and models produced with 2D (red) and 2.5D FWI (black).

516x409mm (300 x 300 DPI)

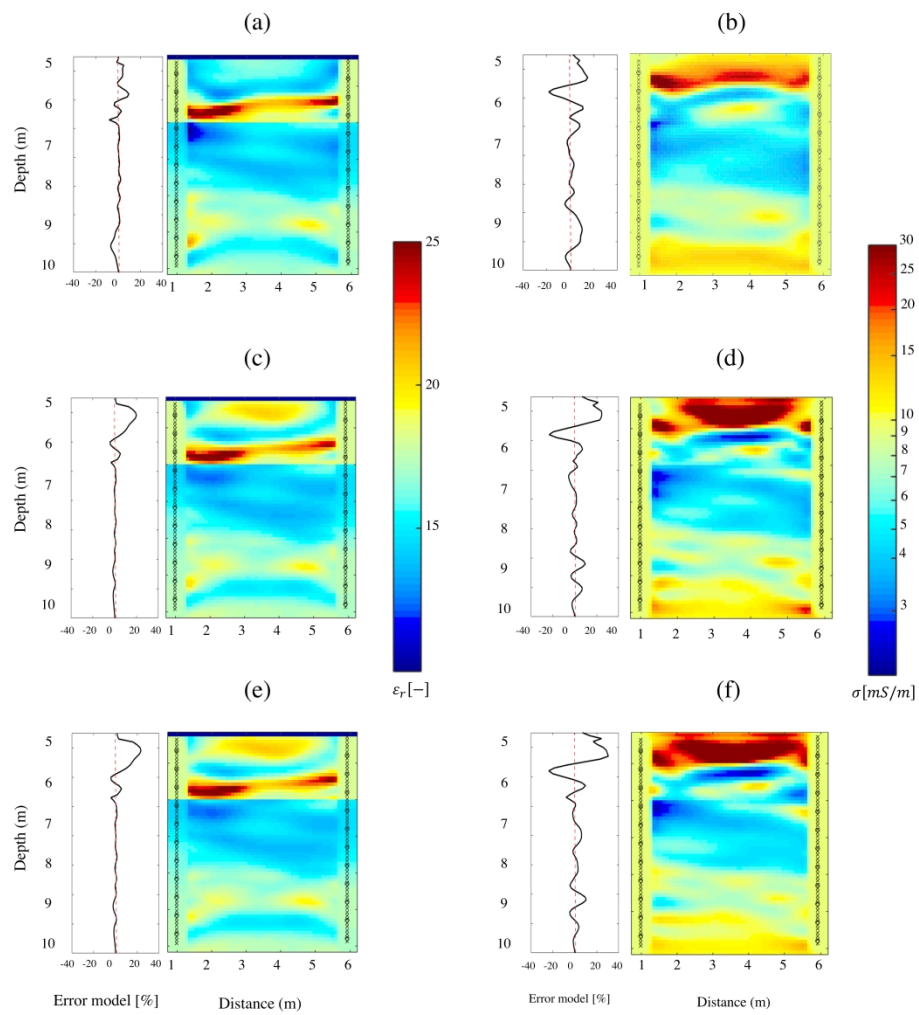


Figure 5 /  $\epsilon_r$  and  $\sigma$  and tomograms produced by 2.5D FWI for different starting models created from the 1st (a and b), 4th (c and d) and 7th (e and f) iteration of 2D FWI. Corresponding lateral average errors are plotted on the right side of each tomogram. Note the logarithmic scale for  $\sigma$  tomograms. Transmitter and receiver positions are indicated by circle and crosses, respectively.

392x425mm (300 x 300 DPI)

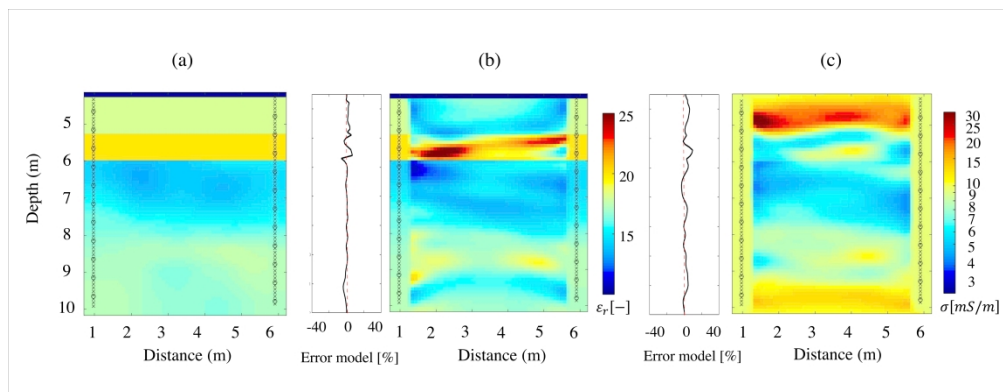


Figure 6 / Updated  $\epsilon_r$  starting model (a),  $\epsilon_r$  (b) and  $\sigma$  (c) resulting tomograms of the 2.5D FWI and the corresponding lateral average model errors on the left side. Note the logarithmic scale for  $\sigma$  tomogram. Transmitter and receiver positions are indicated by circle and crosses, respectively.

652x253mm (300 x 300 DPI)



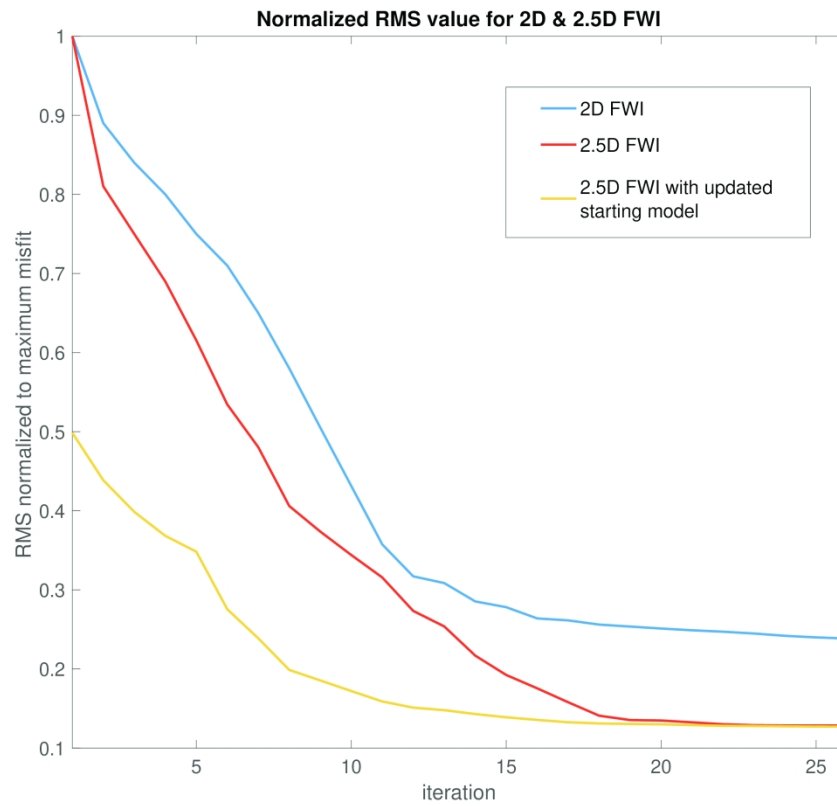


Figure 7 / RMS misfit curves for 2D FWI (blue) and 2.5D FWI (red) using the same starting models, and, the 2.5D FWI using the updated  $\epsilon_r$  starting model. RMS curves are normalized to the starting model value (0 iteration) used for the 2D and 2.5D FWI.

297x260mm (300 x 300 DPI)

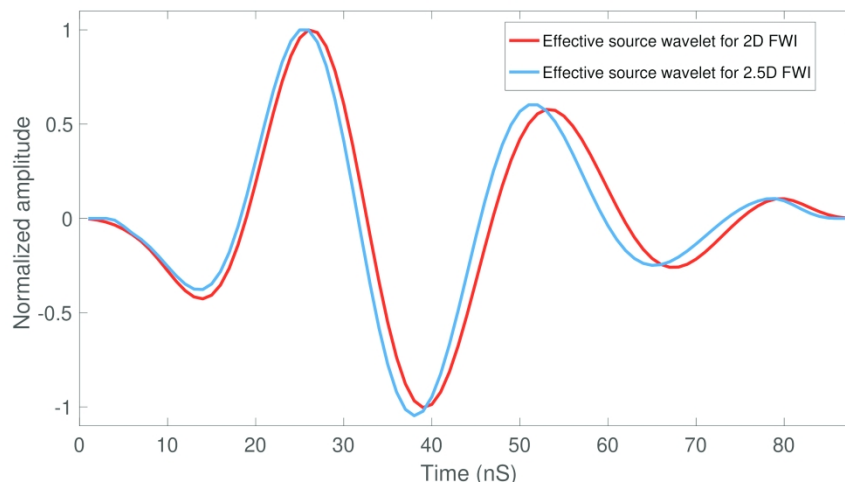


Figure 8 / Comparison of the 2D effective source wavelet based on Klotzsche et al. (2012) in red and the 2.5D effective source wavelet in blue using the deconvolution approach. Note both wavelets are normalized to their maximum amplitude.

351x178mm (300 x 300 DPI)

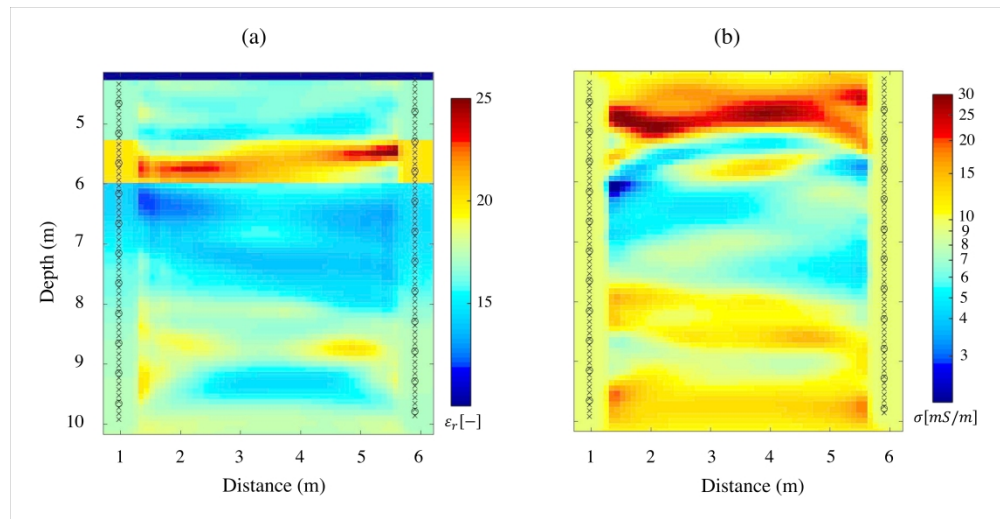


Figure 9 / 2.5D FWI tomograms for  $\epsilon_r$  (a) and  $\sigma$  (b) for the experimental data of the Widen test site using the updated starting model (see Figure 6a) and effective source wavelet (see Figure 8, blue). Note the logarithmic scale for  $\sigma$  tomogram. Transmitter and receiver locations are indicated by circles and crosses, respectively.

638x327mm (300 x 300 DPI)